

A Systematic Small-signal Analysis Procedure for Improving Synchronization Stability of Grid-forming Virtual Synchronous Generators

Francisco Jesús Matas-Díaz, Manuel Barragán-Villarejo, and José María Maza-Ortega

Abstract—The integration of converter-interfaced generators (CIGs) into power systems is rapidly replacing traditional synchronous machines. To ensure the security of power supply, modern power systems require the application of grid-forming technologies. This study presents a systematic small-signal analysis procedure to assess the synchronization stability of grid-forming virtual synchronous generators (VSGs) considering the power system characteristics. Specifically, this procedure offers guidance in tuning controller gains to enhance stability. It is applied to six different grid-forming VSGs and experimentally tested to validate the theoretical analysis. This study concludes with key findings and a discussion on the suitability of the analyzed grid-forming VSGs based on the power system characteristics.

Index Terms—Voltage source converter (VSC), grid-forming controller, virtual synchronous generator (VSG), small-signal stability analysis.

I. INTRODUCTION

THE transition to a power system dominated by renewable energy sources (RESs) interfaced with power electronics converters is an indisputable fact. These new converter-interfaced generators (CIGs) have been installed across all voltage levels, from transmission to distribution networks [1]. This transition makes the modern power system susceptible to large frequency and voltage deviations due to the reduced inertia and damping [2], limited primary frequency response (PFR) stemming from the maximum power point (MPP) operation [3], and new instabilities emerging from CIG dynamics [4]. As a result, the new functionalities of CIGs are required to ensure a safe and reliable operation of the power system [5].

Fortunately, new operation modes of CIGs have been developed to address the technical challenges associated with

large-scale RES integration. Among these, the grid-forming control has gained prominence [6]. Unlike conventional grid-following CIGs, which function as AC current sources, the grid-forming CIGs operate as AC voltage sources. In this manner, the grid-forming controller of CIG is in charge of providing the amplitude, frequency, and phase for this voltage source. To achieve this, the grid-forming controller comprises an outer control loop (OCL) that generates setpoints for the inner control loop (ICL) [7]. The OCL is responsible for controlling the active power to maintain the grid synchronization and the reactive power to regulate the voltage at the point of interconnection (POI). Meanwhile, the ICL is responsible for controlling the voltage and/or current at POI according to the setpoints provided by the OCL. Although most grid-forming controllers of CIG adhere to this hierarchical structure, they differ in terms of specific implementations [7], [8].

The OCLs comprise the active power control loops (APCLs) and reactive power control loops (RPCLs). The most common APCLs for grid synchronization are: ① droop control [9], ② power synchronization control [10], ③ enhanced direct power control [11], ④ synchronverter [12], and ⑤ synchronous power control [13]. The droop control is a well-established technique for microgrids, whereas the power synchronization control is one of the first proposals based on the synchronous generator emulation. The implementation of the synchronverter, i.e., virtual synchronous generator (VSG), is based on the swing equation [14] or a proportional-integral (PI) controller [15], which is termed as S-VSG or PI-VSG for simplicity in this paper, respectively. The primary difference between them is that the PI-VSG allows the inertial response to be independent from the PFR. The synchronous power control computes the VSG angle as a second-order transfer function of the active power error, thereby increasing the flexibility in VSG control. On the other hand, the RPCLs for voltage regulation can be categorized into three types: ① droop control [16], ② PI-based control [17], and ③ cascaded control with droop and PI regulators [18].

Regarding the ICL, various controllers are presented: ① open-loop controller [19], ② single voltage controller [20], ③ single current controller with virtual admittance [21], [22], and ④ cascaded voltage controller with both voltage and current control loops [23]. The main disadvantage of the first two controllers is their lack of current controllability, which can result in overcurrent during events with fast dy-

Manuscript received: March 23, 2024; revised: July 16, 2024; accepted: November 14, 2024. Date of CrossCheck: November 14, 2024. Date of online publication: January 30, 2025.

This work was supported by Grant PID2021-124571OB-I00 funded by MICIU/AEI/10.13039/501100011033 and by FEDER, EU.

This article is distributed under the terms of the Creative Commons Attribution 4.0 International License (<http://creativecommons.org/licenses/by/4.0/>).

F. J. Matas-Díaz, M. Barragán-Villarejo, and J. M. Maza-Ortega (corresponding author) are with the Department of Electrical Engineering, University of Seville, 41004 Seville, Spain (e-mail: fmatas@us.es; manuelbarragan@us.es; jm-maza@us.es).

DOI: 10.35833/MPCE.2024.000316



namics such as short-circuit faults.

The combination of different OCL and ICL blocks results in a plethora of grid-forming controllers of CIGs. Therefore, it is required to assess the performance of these controllers systematically considering the following aspects [7]: ① synchronization stability, ② overcurrent management or fault ride-through capability, and ③ the transition between islanded and grid-connected modes. Focusing on the synchronization stability, it has been shown that the grid-forming CIGs can maintain synchronism in weak grids, but they often fail to maintain stability in stiff grids. This instability arises because even minor phase differences between the CIG and power grid can lead to significant active power fluctuations [24]. Several studies have attempted to address this issue using simplified small-signal impedance models that neglect the ICL dynamics [25]. However, these approaches are inadequate for stability studies [26], as they merely predict the input-output dynamics at the converter terminals without considering how the state variables influence the oscillation modes that determine the system stability margins [27]. Accordingly, [28] proposes a small-signal model with a single-input single-output (SISO) stability analysis approach for a specific CIG implementation. In addition, the stability of grid-forming CIGs has been addressed by small-signal analysis based on state-space models. Using this small-signal analysis technique, [29] evidences that the interaction of feed-forward terms in cascade controllers in the ICL may lead to instability regardless of the grid short-circuit ratio (SCR). However, this analysis does not consider the OCL dynamics, which are crucial for a comprehensive stability analysis, as discussed in [19] and [30]-[33]. These studies show that the grid SCR is a critical parameter that can significantly affect the stability of grid-forming CIGs. The findings of these studies are relevant but it is questionable whether they can be generalized across all the possible combinations of OCL and ICL blocks to implement a grid-forming VSG. Similarly, an analytical design approach for a grid-forming controller based on power synchronization control with a voltage-controlled ICL is presented in [34]. However, this approach uses a specific combination of OCL and ICL blocks that limits its applicability to certain ranges of grid impedances, making it challenging to extend to other types of grid-forming controllers.

However, recent studies suggest that the SCR may not provide accurate estimations of system impedance or strength in converter-dominated power systems. This is mainly because the short-circuit current contributions from voltage source converters (VSCs) and synchronous generators are different. Moreover, it is uncertain how to effectively utilize the SCR information to design the CIG controllers [35], [36]. Despite these recent investigations, the SCR is still being used for characterizing the grid for stability studies [37], but, given the aforementioned uncertainty, modern power systems will require stability analysis covering a wide SCR range.

Considering this background, the specific contributions of this study can be summarized as follows.

1) The stability ranges are identified for different types of grid-forming VSGs based on the value *SCR* and ratio *R/X* of the grid through a small-signal analysis.

2) A systematic procedure is proposed based on the analysis of participation factors, which extends the operating range of grid-forming VSGs by identifying the control state variables with the major weight on the oscillation modes causing system instability.

3) The control loops that cause synchronization instability for each type of grid-forming VSG are identified. This will show that the ICL dynamics of grid-forming VSGs cannot be neglected in the stability analysis.

4) The proposed systematic procedure for improving the synchronization stability of grid-forming VSGs is experimentally validated.

The remainder of this paper is organized as follows. Section II presents the state-space modeling of grid-forming VSGs. Section III outlines the systematic small-signal analysis procedure to evaluate the effects of *SCR* and *R/X* on the stability range, which is applied to a case study. From this analysis, the controller gains are re-tuned to extend the stability range for networks with different characteristics. Section IV describes the experimental validation. Section V discusses considerations and important properties of grid-forming VSGs that should be additionally considered beyond the findings obtained from the small-signal analysis. Section VI concludes by describing the main findings and gives an assessment of the most suitable OCL-ICL combinations based on power system characteristics.

II. STATE-SPACE MODELING OF GRID-FORMING VSGS

This section details the state-space model of a grid-connected VSC and the most common OCLs and ICLs to implement a grid-forming VSG. The differential equations of the grid-forming VSGs are modeled in the *dq* frame, synchronized with the VSG angle θ_{vsg} . The models of the APCL and RPCL are nonlinear. Consequently, the linearization of the state-space model is required prior to implementing the systematic small-signal analysis procedure proposed in Section III.

A. Grid-connected VSC model

The CIG considered in this study is a three-phase three-wire VSC connected to the grid via an LCL coupling filter, which includes a series damping resistor alongside the capacitor, as illustrated in Fig. 1.

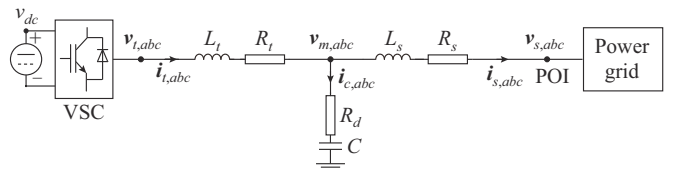


Fig. 1. One-line diagram of a three-phase three-wire grid-connected VSC.

The differential equations for the grid-connected VSC in the *dq* frame are given as:

$$\mathbf{v}_t = R_t \mathbf{i}_t + L_t \frac{d\mathbf{i}_t}{dt} + \omega_{vsg} L_t \mathbf{i}_t + \mathbf{v}_m \quad (1)$$

$$\begin{cases} \dot{\mathbf{i}}_c = C \frac{d\mathbf{v}_m}{dt} + \omega_{\text{vsg}} \mathbf{C} \mathbf{v}_m - CR_d \frac{d\mathbf{i}_c}{dt} \\ \mathbf{i}_c = \mathbf{i}_t - \mathbf{i}_s \end{cases} \quad (2)$$

$$\mathbf{v}_m = R_s \mathbf{i}_s + L_s \frac{d\mathbf{i}_s}{dt} + \omega_{\text{vsg}} \mathbf{L}_s \mathbf{i}_s + \mathbf{v}_s \quad (3)$$

where $\mathbf{v}_t = [v_{td}, v_{tq}]^T$ is the VSC voltage; $\mathbf{v}_m = [v_{md}, v_{mq}]^T$ is the voltage of RC branch; $\mathbf{v}_s = [v_{sd}, v_{sq}]^T$ is the grid-side inductor voltage; $\mathbf{i}_t = [i_{td}, i_{tq}]^T$ is the VSC-side current; $\mathbf{i}_s = [i_{sd}, i_{sq}]^T$ is the grid-side current; and $\mathbf{i}_c = [i_{cd}, i_{cq}]^T$ is the capacitor current; ω_{vsg} is the angular speed of VSG; $\mathbf{L}_t = \begin{bmatrix} 0 & -L_t \\ L_t & 0 \end{bmatrix}$ and $\mathbf{L}_s = \begin{bmatrix} 0 & -L_s \\ L_s & 0 \end{bmatrix}$ are the VSC and grid-side inductances, which are along with inner resistances R_t and R_s , respectively; and R_d and $C = \begin{bmatrix} 0 & -C \\ C & 0 \end{bmatrix}$ are the damping resistance and capacitance of the coupling filter, respectively.

The power grid is modeled based on its Thevenin equivalent as:

$$\mathbf{v}_s = R_g \mathbf{i}_s + L_g \frac{d\mathbf{i}_s}{dt} + \mathbf{L}_g \omega_{\text{vsg}} \mathbf{i}_s + \mathbf{v}_g \quad (4)$$

where $\mathbf{v}_g = [v_{gd}, v_{gq}]^T$ is the grid voltage; and $\mathbf{L}_g = \begin{bmatrix} 0 & -L_g \\ L_g & 0 \end{bmatrix}$ and R_g are the grid inductance and resistance, respectively.

The state-space model of the grid-connected VSC is represented in (1)-(4) and contains six state variables:

$$\mathbf{x}_f = [i_{td} \ i_{tq} \ i_{sd} \ i_{sq} \ v_{md} \ v_{mq}] \quad (5)$$

B. OCLs

Regarding the OCL, the APCL provides the angular speed and angle of virtual rotor, i.e., ω_{vsg} and θ_{vsg} , respectively, whereas the RPCL provides the virtual electromotive force, i.e., E . The OCL control schemes, comprising two possible implementations based on S-VSG [38]-[40] or PI-VSG [15], are shown in Fig. 2(a).

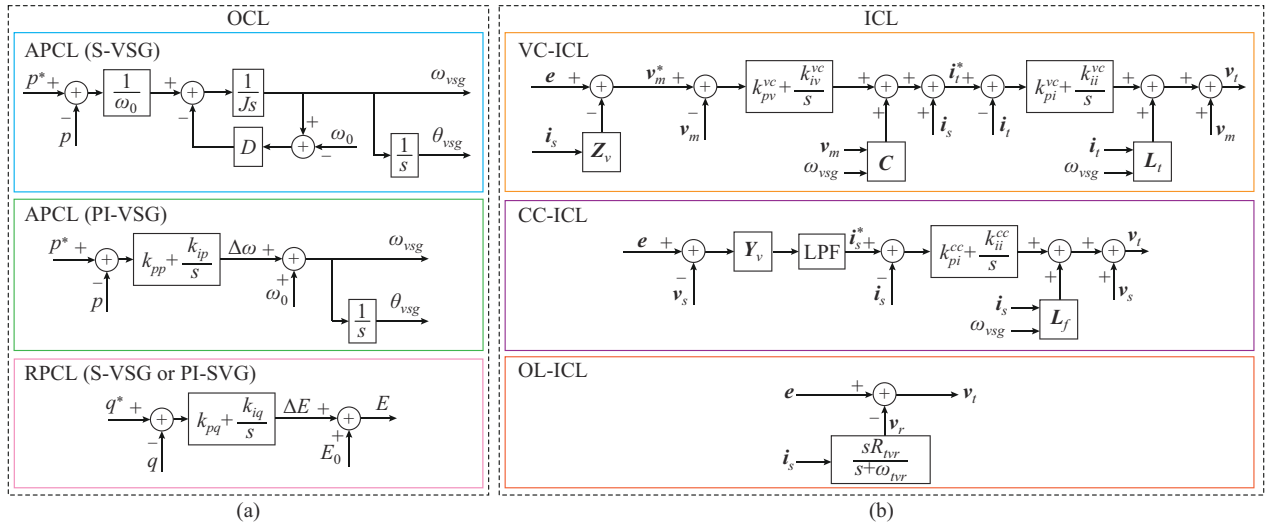


Fig. 2. Diagrams of OCL and ICL blocks considered for analyzed grid-forming VSGs. (a) OCL. (b) ICL.

Both S-VSG and PI-VSG consider that the grid voltage rotates at the nominal frequency ω_0 , which acts as a perturbation with no influence on the system dynamics [41], i.e., ω_0 is a constant parameter. In this manner, the phase difference between the grid voltage θ_g and the electromotive force angle θ_{vsg} can be defined as ψ [42]:

$$\begin{cases} \psi = \theta_g - \theta_{\text{vsg}} \\ \frac{d\psi}{dt} = \omega_0 - \frac{d\theta_{\text{vsg}}}{dt} \end{cases} \quad (6)$$

The OCL formulation based on the S-VSG or PI-VSG is presented as follows.

1) S-VSG

The APCL based on S-VSG can be expressed as:

$$\begin{cases} J\omega_0 \frac{d\omega_{\text{vsg}}}{dt} = p^* - p - D(\omega_{\text{vsg}} - \omega_0) \\ \frac{d\theta_{\text{vsg}}}{dt} = \omega_{\text{vsg}} \end{cases} \quad (7)$$

where p is the measured active power; p^* is the active power

reference, i.e., virtual mechanical power; J is the rotational inertia; and D is the damping coefficient.

Combining (6) and (7) leads to:

$$\begin{cases} J\omega_0 \frac{d\omega_{\text{vsg}}}{dt} = p^* - p + D \frac{d\psi}{dt} \\ \frac{d\psi}{dt} = \omega_0 - \omega_{\text{vsg}} \end{cases} \quad (8)$$

The RPCL consists of a PI controller, which can be formulated as:

$$\begin{cases} E = k_{pq} \frac{d\zeta_q}{dt} + k_{iq} \zeta_q + E_0 \\ \frac{d\zeta_q}{dt} = q^* - q \end{cases} \quad (9)$$

where ζ_q is the integral of reactive power error; q is the measured reactive power; q^* is the reactive power reference; E_0 is the rated electromotive force; and k_{pq} and k_{iq} are the proportional and integral gains of PI controller in the RPCL, respectively.

Therefore, the S-VSG introduces three state variables in the state-space model:

$$\mathbf{x}_{s-vsg} = \begin{bmatrix} \psi & \omega_{vsg} & \zeta_q \end{bmatrix}^T \quad (10)$$

2) PI-VSG

The APCL based on PI-VSG, consisting of a PI controller applied to the active power error, can be written as:

$$\begin{cases} \frac{d\psi}{dt} = -k_{pp} \frac{d\zeta_p}{dt} - k_{ip} \zeta_p \\ \frac{d\zeta_p}{dt} = p^* - p \end{cases} \quad (11)$$

where ζ_p is the integral of active power error; and k_{pp} and k_{ip} are the proportional and integral gains of PI controller in the APCL, respectively.

The RPCL of PI-VSG is identical to that of the S-VSG. Therefore, the PI-VSG introduces three state variables in the state-space model:

$$\mathbf{x}_{pi-vsg} = \begin{bmatrix} \psi & \zeta_p & \zeta_q \end{bmatrix}^T \quad (12)$$

C. ICLs

Three types of ICLs are considered for the grid-forming VSG: ① voltage controller by means of cascaded controller [24], ② current controller with a virtual admittance [21], and ③ an open-loop voltage controller [19], which are termed as VC-ICL, CC-ICL, and OL-ICL for simplicity, respectively. The control scheme for each type of ICL is shown in Fig. 2(b).

1) VC-ICL

A cascaded voltage controller composed of voltage and current control loops is used to control the capacitor voltage of the LCL filter. The voltage reference of RC branch \mathbf{v}_m^* is computed as [43]:

$$\mathbf{v}_m^* = \mathbf{e} - \mathbf{Z}_v \mathbf{i}_s \quad (13)$$

where $\mathbf{Z}_v = \begin{bmatrix} R_v & -X_v \\ X_v & R_v \end{bmatrix}$ is the virtual impedance; and $\mathbf{e} = [0, -E]$ is the virtual electromotive force computed by the RP-CL.

A PI voltage controller provides the setpoints to the current control loop:

$$\begin{cases} \mathbf{i}_t^* = k_{pv} \frac{d\zeta_v}{dt} + k_{iv}^vc \zeta_v + \omega_{vsg} \mathbf{C} \mathbf{v}_m + \mathbf{i}_s \\ \frac{d\zeta_v}{dt} = \mathbf{v}_m^* - \mathbf{v}_m \end{cases} \quad (14)$$

where $\zeta_v = [\zeta_{vd}, \zeta_{vq}]^T$ is the integral of the voltage error; \mathbf{i}_t^* is the VSC-side current reference; and k_{pv}^vc and k_{iv}^vc are the proportional and integral gains of the PI voltage controller in VC-ICL, respectively.

The tracking of \mathbf{i}_t^* is carried out in the current control loop, which is based on a PI current controller and modeled as:

$$\begin{cases} \mathbf{v}_r = k_{pi}^vc \frac{d\zeta_i}{dt} + k_{ii}^vc \zeta_i + \omega_{vsg} \mathbf{L}_j \mathbf{i}_t + \mathbf{v}_m \\ \frac{d\zeta_i}{dt} = \mathbf{i}_t^* - \mathbf{i}_t \end{cases} \quad (15)$$

where $\zeta_i = [\zeta_{id}, \zeta_{iq}]^T$ is the integral of the current error; and k_{pi}^vc and k_{ii}^vc are the proportional and integral gains of the PI current controller in VC-ICL, respectively.

Based on (13)-(15), the VC-ICL adds four new state variables to the state-space model:

$$\mathbf{x}_{vc} = \begin{bmatrix} \zeta_{vd} & \zeta_{vq} & \zeta_{id} & \zeta_{iq} \end{bmatrix}^T \quad (16)$$

2) CC-ICL

CC-ICL controls the grid-side inductor current of LCL filter. To achieve this, a PI controller is applied to the current error. The grid-side current reference \mathbf{i}_s^* is obtained using a virtual admittance and a low-pass filter (LPF) as:

$$\mathbf{i}_s^{vsg} = \mathbf{Y}_v (\mathbf{e} - \mathbf{v}_s) \quad (17)$$

$$\mathbf{i}_s^{vsg} = \tau_{lpf} \frac{d\mathbf{i}_s^*}{dt} + \mathbf{i}_s^* \quad (18)$$

where τ_{lpf} is the time constant of LPF; \mathbf{i}_s^{vsg} is the input current of LPF; and $\mathbf{Y}_v = \begin{bmatrix} G_v & B_v \\ -B_v & G_v \end{bmatrix}$ is the virtual admittance matrix, with G_v and B_v being the virtual conductance and susceptance, respectively. The differential equations of the PI current controller, including the cross-coupling cancellation and feed-forward terms, are expressed as:

$$\begin{cases} \mathbf{v}_r = k_{pi}^{cc} \frac{d\zeta_i}{dt} + k_{ii}^{cc} \zeta_i + \omega_{vsg} \mathbf{L}_j \mathbf{i}_s + \mathbf{v}_s \\ \frac{d\zeta_i}{dt} = \mathbf{i}_s^* - \mathbf{i}_s \end{cases} \quad (19)$$

where $\mathbf{L}_j = \mathbf{L}_l + \mathbf{L}_s$; and k_{pi}^{cc} and k_{ii}^{cc} are the proportional and integral gains of the PI current controller in CC-ICL, respectively.

Therefore, based on (17)-(19), the CC-ICL adds four state variables to the state-space model:

$$\mathbf{x}_{cc} = \begin{bmatrix} \mathbf{i}_{sd}^* & \mathbf{i}_{sq}^* & \zeta_{id} & \zeta_{iq} \end{bmatrix}^T \quad (20)$$

3) OL-ICL

The OL-ICL directly applies the virtual electromotive force E to the VSC terminals. A slight modification of E is proposed using a transient virtual resistor (TVR) to provide more damped current dynamics [39]. The TVR consists of a first-order high-pass filter, which is formulated as:

$$R_{tvr} \frac{d\mathbf{v}_r}{dt} = \frac{d\mathbf{v}_r}{dt} + \omega_{tvr} \mathbf{v}_r \quad (21)$$

where $\mathbf{v}_r = [v_{rd}, v_{rq}]^T$ is the output voltage of TVR; and R_{tvr} and ω_{tvr} are the gain and cut-off frequency of high-pass filter, respectively. Then, the VSC terminal voltage is computed as:

$$\mathbf{v}_t = \mathbf{e} - \mathbf{v}_r \quad (22)$$

The OL-ICL introduces two new state variables to the state-space model:

$$\mathbf{x}_{ol} = \begin{bmatrix} v_{rd} & v_{rq} \end{bmatrix}^T \quad (23)$$

It is important to note that for different ICLs, the power terms used in the corresponding OCL blocks are computed at different nodes, i.e., at the capacitor branch of LCL filter for the VC-ICL, at the POI for the CC-ICL, and at the VSC

terminals for the OL-ICL.

Therefore, six state-space models of grid-forming VSG are derived based on the selected OCL and ICL blocks, which can be formulated in a generalized form as:

$$\begin{cases} \dot{\mathbf{x}}_{\text{OCL-ICL}} = \mathbf{A}\mathbf{x}_{\text{OCL-ICL}} + \mathbf{B}\mathbf{u} \\ \mathbf{u} = [p^* \quad q^*] \end{cases} \quad (24)$$

where \mathbf{A} and \mathbf{B} are the state-space matrices; and the state vector $\mathbf{x}_{\text{OCL-ICL}}$ is composed of the state variables of grid-connected VSC in (5), the state variables of OCL in (10) or (12), and state variables of ICL in (16), (20), or (23).

III. SYSTEMATIC SMALL-SIGNAL ANALYSIS PROCEDURE FOR SYNCHRONIZATION STABILITY

This section presents a systematic small-signal analysis procedure to ensure the synchronization stability and good dynamic performance of the grid-forming VSGs in power systems with different SCR and R/X .

A. Proposed Systematic Procedure

This subsection presents the steps of the proposed systematic procedure for improving the synchronization stability of grid-forming VSGs. The fundamentals of the small-signal analysis are presented in Supplementary Material A. The proposed systematic procedure consists of the following steps.

Step 1: validate the linear model against the original nonlinear model by comparing the dynamic performance of some key magnitudes, such as the active and reactive power used in the OCL.

Step 2: identify stable and unstable regions over a wide range of SCR and R/X through a small-signal analysis based on the linear model.

Step 3: identify the eigenvalues associated with the critical oscillation modes at the boundary between stable and unstable regions. These eigenvalues are those that lead the system to unstable operation.

Step 4: based on these critical oscillation modes, detect the critical state variables by analyzing their corresponding participation factors for the unstable region identified in *Step 3*. In particular, the critical state variables are those with the largest participation factors in the critical oscillation modes. Detailed information on the computation and interpretation of participation factors can be found in Supplementary Material A.

Step 5: perform a sensitivity analysis of the controller gains associated with the critical state variables within the unstable region identified in *Step 3* to increase the synchronization stability range of the grid-forming VSG.

B. Case Study

This subsection presents a case study using a CIG with the parameters shown in Table I to illustrate the application of the proposed systematic procedure. The controller gains of the grid-forming VSG are selected according to the state of the art. Specifically, the APCL and RPCL gains of PI-VSG as well as the control parameters of CC-ICL are obtained from [42]. The S-VSG gains are calculated following [15], considering the same inertia constant as that of the PI-VSG and a damped response. The TVR in the OL-ICL is obtained from [39], the VC-ICL gains are computed using the

best pole location [24], and the virtual impedance is calculated using a sensitivity analysis [42]. The equilibrium point \mathbf{x}_0 is used to linearize the system considering the input vector $\mathbf{u}_0 = [9 \text{ kW}, 4.5 \text{ kvar}]$.

TABLE I
SYSTEM PARAMETERS FOR CASE STUDY

Parameter	Value	Parameter	Value
L_t (mH)	1.25	X_v (Ω)	0.08
R_t (Ω)	0.04	k_{ip} (rad/s·W ⁻¹)	0.0016
L_s (mH)	1.25	D (sNm/rad)	47.36
R_s (Ω)	0.04	k_{iq} (V/W)	0.0163
R_v (Ω)	0	ω_{nr} (rad/s)	60
k_{pp} (rad/s·W ⁻¹)	0.0012	τ_{ipf} (ms)	1.6
J (kg·m ²)	2.03	k_{pi}^{cc} (V/A)	1.25
k_{pq} (V/W)	0.0016	k_{ii}^{cc} (V/A)	40
R_{nr} (Ω)	0.09	G_v (S)	0
ω_0 (rad/s)	100 π	B_v (S)	1.25
R_d (Ω)	10	k_{pv}^{vc} (A/V)	0.1
C_f (μ F)	4	k_{iv}^{vc} (A/V)	0.1
E_0 (V)	230 $\sqrt{2}$	k_{pi}^{vc} (V/A)	0.1
V_g (V)	230 $\sqrt{2}$	k_{ii}^{vc} (V/A)	15.1

Step 1: the linear model is validated by comparing its step response with that of the nonlinear model. Figure 3 compares the step response of linear and nonlinear models with active and reactive power step changes of $\Delta p^* = 0.5 \text{ kW}$ and $\Delta q^* = 0.5 \text{ kvar}$, respectively, with respect to the input vector \mathbf{u}_0 .

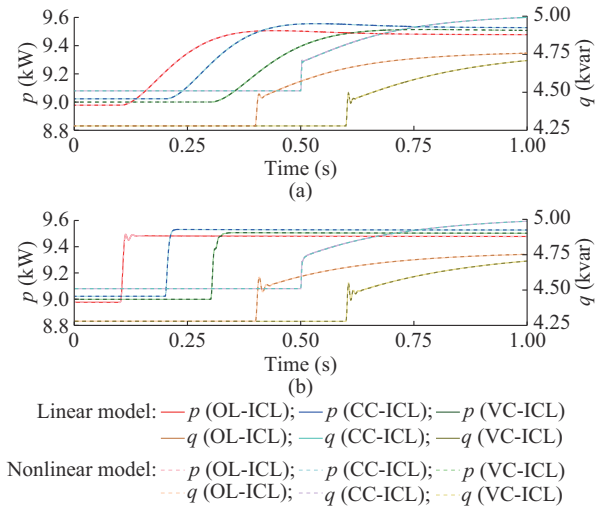


Fig. 3. Step response of linear and nonlinear models to active and reactive power step changes of $\Delta p^* = 0.5 \text{ kW}$ and $\Delta q^* = 0.5 \text{ kvar}$. (a) S-VSG. (b) PI-VSG.

The active power and reactive power are computed at the midpoint of the LCL filter to which the capacitor is connected. The active and reactive power step changes are applied to all the combinations of OCL and ICL blocks at different time instants in a compact manner without overlaps. In addition, note that the steady-state active power and reactive power for each ICL are different, since the power involved in the OCL depends on the implemented ICL, as previously

described in Section II. Figure 3 demonstrates that all the linear models accurately match the dynamics of the respective nonlinear models. Therefore, it is possible to perform a rigorous stability and dynamic performance analysis using the linear models.

Step 2: the objective of this step is to evaluate the stability of the six grid-forming VSGs with different combinations of OCL and ICL blocks in different power grids. According to the implemented OCL and ICL blocks, the six grid-forming VSGs can be termed as S-VC, S-CC, S-OL, PI-VC, PI-CC, and PI-OL. A wide range of SCR and R/X is used to characterize different power grids. According to the standard IEEE Std. 1204-1997 [44], the threshold between a strong and a weak grid can be set to be $SCR=3$, which means that a system is very weak when $SCR<3$ and very strong when

$SCR>3$. In addition, the standard IEEE Std. 519-2014 [45] assigns typical ranges to high-voltage (HV), medium-voltage (MV), and low-voltage (LV) networks based on the ratio between the maximum short-circuit current and the maximum demand load current for the fundamental frequency at the POI. This ratio can be considered identical to SCR for rated voltage values, so the SCR ranges for HV, MV, and LV grids are: $SCR_{HV} \in [0, 50]$, $SCR_{MV} \in [0, 1000]$, and $SCR_{LV} \in [0, 1000]$, respectively. Therefore, the performance of the six grid-forming VSGs is evaluated with $SCR \in [1, 800]$ and $R/X \in [0.06, 1.91]$, which covers all the voltage levels. Figure 4 illustrates the stable region for the six grid-forming VSGs within these intervals.

Figure 4 also illustrates areas that correspond to HV, MV, and LV grids with pairs of SCR and R/X based on [45].

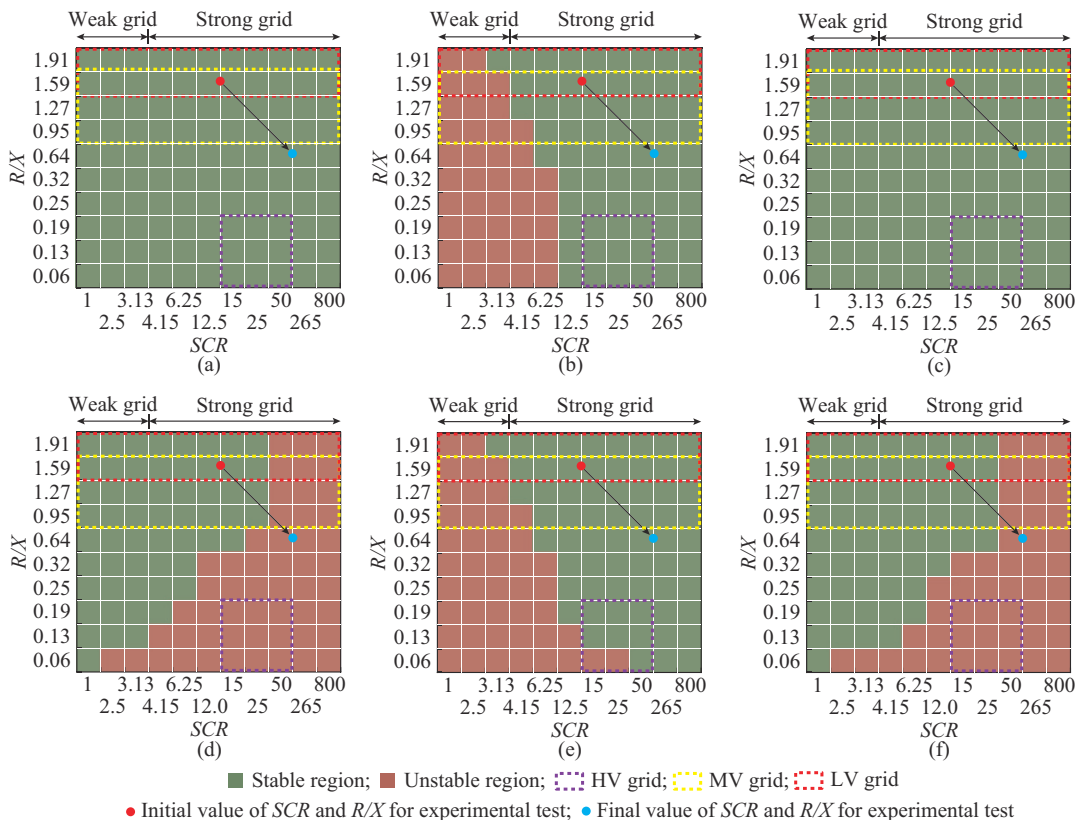


Fig. 4. Stable region for six grid-forming VSGs within $SCR \in [1, 800]$ and $R/X \in [0.06, 1.91]$. (a) S-VC. (b) S-CC. (c) S-OL. (d) PI-VC. (e) PI-CC. (f) PI-OL.

The results for the PI-VSG show that the ICLs based on voltage control, i.e., PI-OL and PI-VC, are generally stable for LV grids, i.e., with high R/X , except for very high SCR . This stability is compromised when the power grid becomes inductive for $R/X<0.19$, regardless of SCR . In addition, it is observed that both PI-OL and PI-VC are unstable when $SCR>25$ regardless of R/X . This means that PI-OL and PI-VC are not recommended for CIGs connected to grids with low impedance and/or high reactance, i.e., HV grids. Regarding the PI-CC, the system is stable with medium/high SCR and medium/low R/X , i.e., HV and MV grids, achieving full stability for $SCR>25$ regardless of R/X . In addition, a large R/X contributes to the system stability, irrespective of SCR .

This suggests that PI-CC is not suitable for networks with high impedance and/or high reactance. In the case of the S-VSG, the ICLs based on voltage control, i.e., S-VC and S-OL, follow a similar pattern to PI-VC and PI-OL. However, they guarantee stability across the entire range of SCR and R/X . This does not happen in the S-CC, whose performance is very similar to the PI-CC, but achieving a wider stable region for $SCR>6.25$ regardless of R/X . This analysis derives that the performance is similar among the following groups of grid-forming VSGs: ① PI-OL and PI-VC, ② PI-CC and S-CC, and ③ S-OL and S-VC. In addition to the information provided by this small-signal stability analysis, it is possible to provide some physical insights about the perfor-

mance of these groups. PI-OL and PI-VC perform like voltage sources. Accordingly, their stability deteriorates in stiff networks with high SCR , as two voltage sources coupled via a small impedance may experience significant active power variations due to minor phase differences. In this regard, increasing the coupling impedance, i.e., reducing SCR , the stable region of the system widens. By contrast, PI-CC and S-CC behave like a current source from the view of synchronization. They may perform well when connected to stiff grids but deteriorate in weak grids with low SCR . The performances of S-OL and S-VC are similar to their counterparts based on the PI-VSG, i.e., PI-OL and PI-VC, respectively. However, due to the selected damping coefficient D , they offer a fully stable operation within the analyzed intervals of SCR and R/X . For this reason, no further steps of the proposed procedure are applied to these grid-forming VSGs.

Step 3: according to Fig. 4, the boundaries between the stable and unstable regions are clearly identified for each grid-forming VSG. The pair of $SCR=25$ and $R/X=0.32$ is chosen as a representative point to identify the eigenvalues that cause the system to become unstable for PI-OL and PI-VC. This instability is related to the eigenvalues with positive real parts, i.e., λ_5 and λ_6 , as shown in Table II.

TABLE II
CRITICAL OSCILLATION MODES OF GRID-FORMING VSGs

VSG	SCR	R/X	Eigenvalue	$\text{Re}(\lambda)$	f_k (Hz)	ζ_k
PI-OL	25.00	0.32	λ_5, λ_6	14.92	67.21	-0.035
PI-VC	25.00	0.32	λ_5, λ_6	27.80	97.59	-0.045
PI-CC	6.25	0.32	λ_3, λ_4	5.40	1140.00	-0.001
S-CC	6.25	0.32	λ_3, λ_4	14.54	1140.00	-0.002

Table II also lists the frequency f_k and damping ζ_k of the oscillation mode associated with this pair of complex eigenvalues. Note that the frequencies of the critical oscillation mode are below 100 Hz for both PI-OL and PI-VC. In the case of PI-CC and S-CC, the instability is analyzed using

the pair of $SCR=6.25$ and $R/X=0.32$. For these two grid-forming VSGs, the eigenvalues with positive real parts that cause system instability are λ_3 and λ_4 , with the frequency of this critical oscillation mode exceeding 1000 Hz, as shown in Table II.

Step 4: once the critical oscillation modes of each grid-forming VSG have been identified, an in-depth analysis is performed within the boundary between the stable and unstable regions. Figure 5(a) represents the evolution of the eigenvalues associated with the critical oscillation mode of PI-OL, i.e., λ_5 and λ_6 , when SCR increases from 1 to 800 and R/X decreases from 1.91 to 0.06. Note that, according to Fig. 4, these variations shift the system from a stable to an unstable region, which is confirmed in Fig. 5, as the real parts of λ_5 and λ_6 become positive. Table III shows the participation factors of state variables x related to the analyzed grid-forming VSGs for both stable and unstable scenarios. In the case of PI-OL, the participation factor of the state variable ψ in the oscillation mode associated with λ_5 and λ_6 is the largest one in the unstable scenario of $SCR=800$ and $R/X=0.06$. This means that ψ is the state variable with the highest contribution to this unstable mode. This state variable is associated with the APCL in the OCL, which is consistent with the low-frequency oscillation mode of λ_5 and λ_6 , as the OCL has slow dynamics. These conclusions can be extended to the PI-VC, which has a similar performance to the PI-OL, as depicted in Table III.

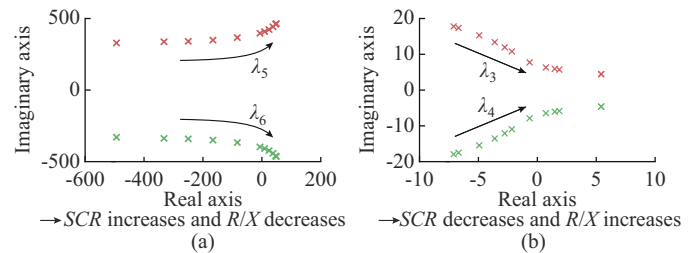


Fig. 5. Evolution of eigenvalues associated with critical oscillation mode of PI-OL and PI-CC when SCR and R/X change. (a) PI-OL. (b) PI-CC.

TABLE III
PARTICIPATION FACTORS OF STATE VARIABLES RELATED TO GRID-FORMING VSGs FOR BOTH STABLE AND UNSTABLE SCENARIOS

x	Participation factor							
	PI-OL (λ_5, λ_6)		PI-VC (λ_5, λ_6)		PI-CC (λ_3, λ_4)		S-CC (λ_3, λ_4)	
	$SCR=1, R/X=1.91$ (stable)	$SCR=800, R/X=0.06$ (unstable)	$SCR=1, R/X=1.91$ (stable)	$SCR=800, R/X=0.06$ (unstable)	$SCR=800, R/X=1.91$ (stable)	$SCR=1, R/X=0.06$ (unstable)	$SCR=800, R/X=1.91$ (stable)	$SCR=1, R/X=0.06$ (unstable)
ψ	0.03	0.18	0.03	0.23	0	0	0	0
ω							0	0
ζ_p	0	0	0	0	0	0		
ζ_q	0	0	0	0.01	0	0	0	0
ζ_{vd}			0	0				
ζ_{vq}			0	0				
i_{sd}^*					0	0.18	0	0.18
i_{sq}^*					0	0.18	0	0.18
ζ_{id}			0	0	0	0	0	0
ζ_{iq}			0	0	0	0	0	0
v_{rd}	0.01	0.03						
v_{rq}	0.01	0.03						

Similarly, the sensitivity analysis of the critical oscillation mode of the PI-CC associated with the complex eigenvalues λ_3 and λ_4 is shown in Fig. 5(b). The evaluation range is identical to that of the PI-OL, but both SCR and R/X decrease, from 800 to 1 and 1.91 to 0.06, respectively, to move from a stable region to an unstable region according to Fig. 4. At the initial values of $SCR=800$ and $R/X=1.91$, the system is stable and then tends to instability as the SCR and R/X decrease. In this case, the state variables with the largest participation factors are i_{sd}^* and i_{sq}^* , as shown in Table III. These state variables correspond to the filtered current references obtained from the virtual admittance in (17) and (18) in the ICL. This result is consistent with the oscillation mode associated with eigenvalues λ_3 and λ_4 , as the ICL is characterized by fast dynamics. This analysis can be extended to the S-CC because its performance is very similar to that of the PI-CC.

Step 5: the aim of this step is to increase the stability range and improve the dynamic performance of grid-forming VSGs affected by the network impedance variation. This is accomplished by re-tuning the controller gains based on the small-signal analysis.

The stability problems of the PI-OL and PI-VC are related to the APCL in OCL; therefore, according to (11), re-tuning their PI controller gains is logical. The proportional gain k_{pp} is modified, as the integral gain k_{ip} is directly related to the inertia constant, i.e., $k_{ip}=1/(2H)$ and cannot be modified so that the VSG inertial response remains unaffected. Figure 6 shows how the eigenvalues λ_5 and λ_6 , related to the critical oscillation modes of the PI-OL and PI-VC, shift to the left when k_{pp} decreases from 1.2×10^{-3} to 7.8×10^{-5} rad/s·W⁻¹, thereby stabilizing the system and progressively increasing the damping of this oscillation mode. $SCR=25$ and $R/X=0.32$ are selected to represent the boundary between the stable and unstable regions used in *Step 3*. In addition, it is also observed that the eigenvalues λ_7 and λ_8 become complex and a new low-frequency oscillation mode at approximately 2 Hz appears when $k_{pp}=2.5 \times 10^{-4}$ rad/s·W⁻¹. From this analysis, the new proportional gain is set to be $k_{pp}=2.5 \times 10^{-4}$ rad/s·W⁻¹, ensuring greater damping of λ_5 and λ_6 without exciting λ_7 and λ_8 .

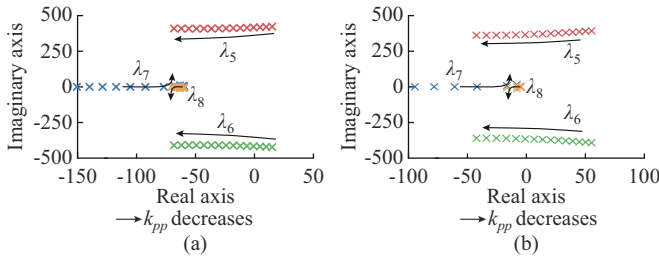


Fig. 6. Evolution of eigenvalues for PI-OL and PI-VC when k_{pp} decreases. (a) PI-OL. (b) PI-VC.

The instability of S-CC and PI-CC is fundamentally different because the root of this problem lies within the virtual admittance and its LPF. Therefore, the targeted control parameters to be re-tuned are G_v , B_v , and τ_{lpf} . Note that increasing G_v destabilizes the system, whereas decreasing B_v and/or increasing τ_{lpf} have a stabilizing effect [42]. The eigenvalue analysis is performed using the grid parameters given in

Step 3, with $SCR=6.25$ and $R/X=0.32$. In this regard, Fig. 7(a) shows that, for the PI-CC, the eigenvalues λ_3 , λ_4 , λ_7 , and λ_8 shift to the left when B_v decreases from 12.5 to 0.25 S. By contrast, λ_5 and λ_6 shift to the right, leading to an oscillation mode with lower natural frequency and damping. A similar changing trend of eigenvalues λ_3 - λ_6 occurs when τ_{lpf} increases from 0.8 to 5.4 ms, as shown in Fig. 7(b). Regarding λ_7 and λ_8 , they follow a curved trajectory and begin moving to the right when $\tau_{lpf}=4$ ms. From this analysis, the selected control parameters for PI-CC and S-CC are $\tau_{lpf}=2.4$ ms and $B_v=0.25$ S.

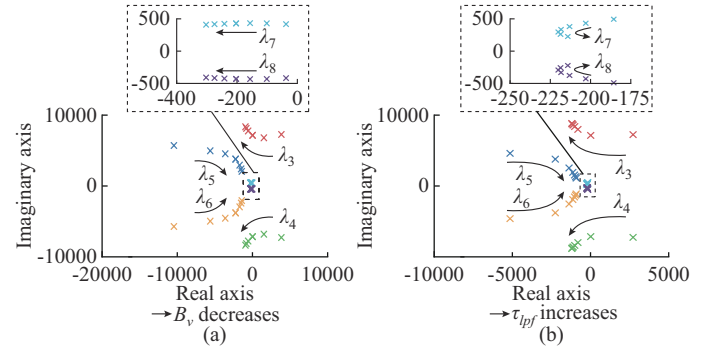


Fig. 7. Evolution of eigenvalues for PI-CC. (a) B_v decreases. (b) τ_{lpf} increases.

These re-tuned control parameters significantly extend the stable region for all grid-forming VSGs, as shown in Fig. 8.

IV. EXPERIMENTAL RESULTS

This section aims to experimentally validate the stability and dynamic response of the grid-forming VSGs to sudden changes in grid impedance.

The experimental validation of the six grid-forming VSGs is conducted using a testbed based on the single-line diagram shown in Fig. 9. It consists of a three-phase three-wire VSC supplied from a 750 V DC voltage source. The VSC setpoints are the same as those used in the theoretical analysis, namely, $\mathbf{u}_0 = [9 \text{ kW}, 4.5 \text{ kvar}]$. The controller gains are listed in Table I considering the re-tuning process. The VSC is connected through an LCL filter to a grid composed of two radial feeders supplied by a controllable AC source with a phase-neutral voltage of 230 V and a frequency of 50 Hz.

The experimental tests evaluate the stability of different grid-forming VSGs against variations in the grid impedance. Initially, in scenario *A*, the contactor N1 is closed and N2 is open, and the power system is characterized by $SCR_A=10$ and $(R/X)_A=1.59$. At a given time, the contactor N2 is closed, connecting both feeders in parallel, namely scenario *B*. This drastically changes the power system characteristics to $SCR_B=90$ and $(R/X)_B=0.65$. The initial and final SCR and R/X for experimental test are marked in Figs. 4 and 8.

The evolution of the active and reactive power of each grid-forming VSG is presented in Fig. 10. At the beginning of the tests (scenario *A*), all the grid-forming VSGs adequately track the power setpoints. The corresponding injected currents are shown in Fig. 11.

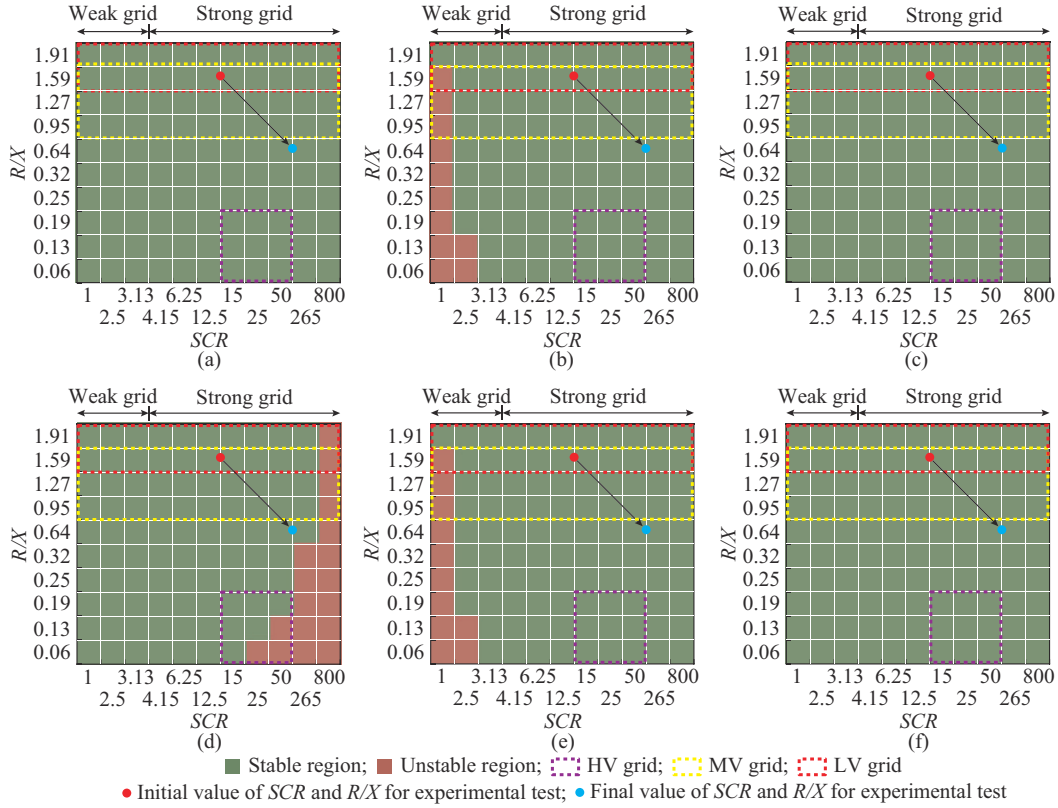


Fig. 8. Stable region with re-tuned control parameters. (a) S-VC. (b) S-CC. (c) S-OL. (d) PI-VC. (e) PI-CC. (f) PI-OL.

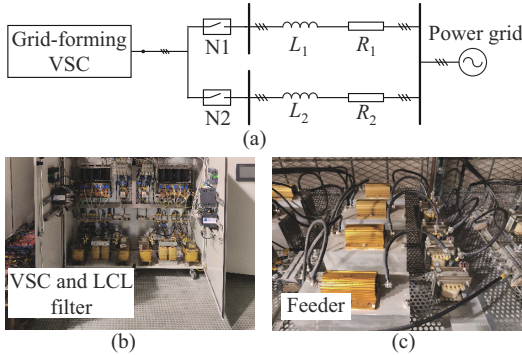


Fig. 9. Experimental testbed. (a) One-line diagram. (b) VSC and LCL filter. (c) Feeder.

Then, the contactor N2 is closed at $t=0.25$ s (scenario B), resulting in a transient response in each grid-forming VSG before they return to their corresponding setpoints. First, the analyzed grid-forming VSGs are stable, as indicated in the theoretical analysis, because the change of power system characteristics is within the identified stable region depicted in Fig. 8. Second, even though each grid-forming VSG exhibits a particular transient response, some conclusions can be drawn based on the implemented ICL block. Those implementations relying on voltage control (OL-ICL and VC-ICL) exhibit an under-damped response with a significant power overshoot. This effect is much more noticeable in the PI-VC, which may lead to undesired VSC overcurrent, as shown in Fig. 11. By contrast, the S-CC and PI-CC show a well-damped response with a slight disturbance when the grid SCR changes.

This experimental performance aligns with the small-signal analysis results, as presented in Table IV. When the power system characteristics of the experimental tests are considered, the critical oscillation modes reveal that voltage-controlled ICLs (OL-ICL and VC-ICL) exhibit lower damping after the power system changes, leading to larger transients. The small-signal analysis results for the S-CC and PI-CC are fully aligned with the experimental test given the large damping after the change in power system characteristics.

V. DISCUSSION

This section discusses some other features, in addition to synchronization stability, of the analyzed grid-forming VSGs that must be considered. These features depend on the implemented OCL and ICL blocks and their corresponding parameterization. In this regard, the fact that the initial settings of the controllers analyzed in this study are chosen according to the state of the art must be highlighted.

Regarding the OCL, the S-VSG leads to wider stability areas compared with PI-VSG, even the PI-VSG gains are tuned, as shown in Fig. 8. The reason is that, although both S-VSG and PI-VSG have the same inertia constant, the S-VSG is parameterized with a value of the damping coefficient D , which results in a larger damping for the S-VSG compared with that achieved by the proportional gain k_{pp} in the PI-VSG. However, this superior performance of the S-VSG in terms of synchronization stability is accompanied by two major drawbacks.

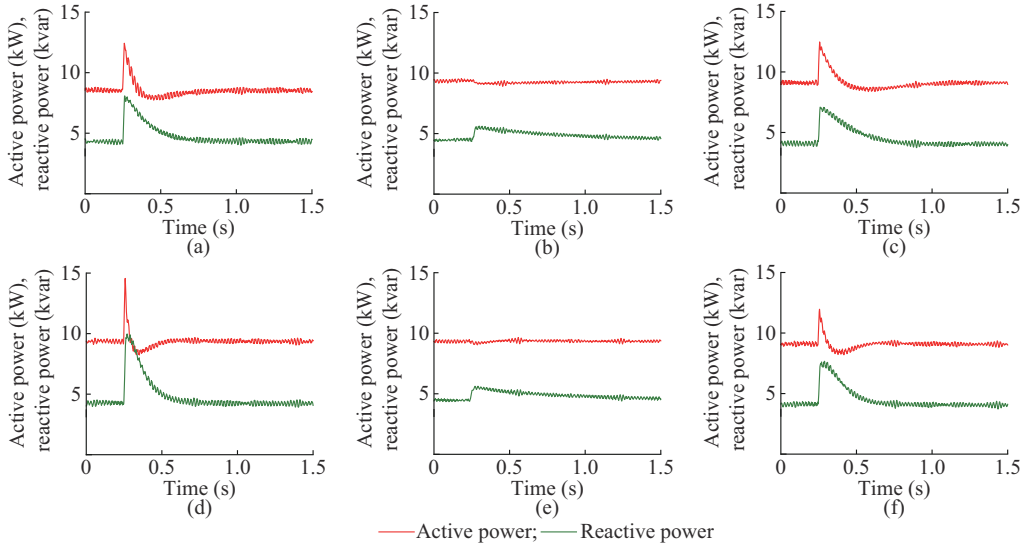


Fig. 10. Evolution of active and reactive power of each grid-forming VSG. (a) S-VC. (b) S-CC. (c) S-OL. (d) PI-VC. (e) PI-CC. (f) PI-OL.

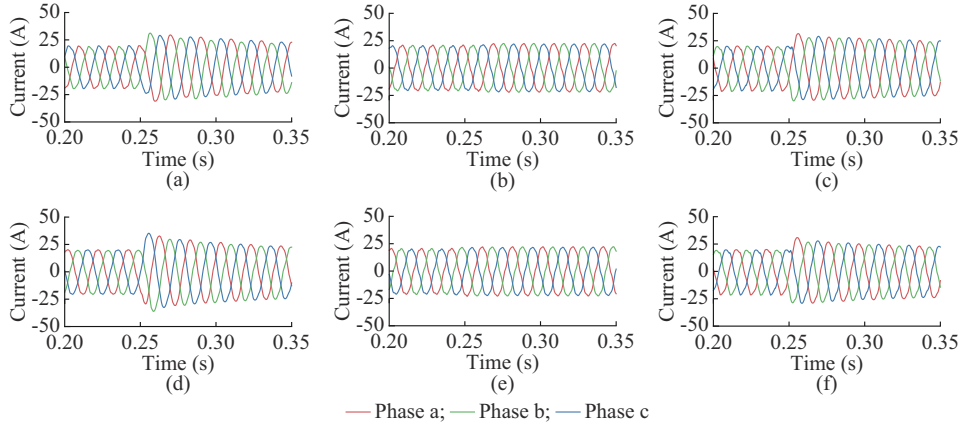


Fig. 11. Evolution of injected current of each grid-forming VSG. (a) S-VC. (b) S-CC. (c) S-OL. (d) PI-VC. (e) PI-CC. (f) PI-OL.

 TABLE IV
 CRITICAL OSCILLATION MODES FOR SMALL-SIGNAL ANALYSIS OF
 EXPERIMENTAL TEST

VSG	Mode	Scenario A		Scenario B	
		f_k (Hz)	ζ_k	f_k (Hz)	ζ_k
S-VC	λ_5, λ_6	57.5	0.498	58.8	0.125
S-CC	λ_3, λ_4	2084.6	0.253	2668.1	0.339
S-OL	λ_5, λ_6	64.6	0.464	68.7	0.176
PI-VC	λ_5, λ_6	55.8	0.470	59.0	0.024
PI-CC	λ_3, λ_4	2084.9	0.253	2668.5	0.339
PI-OL	λ_5, λ_6	63.4	0.442	68.3	0.121

First, the damping and PFR in the S-VSG are coupled, making it impossible to define these two design parameters separately without introducing additional modifications into the APCL. Thus, a large damping coefficient D , which is required because of the POI characteristics, may lead to a large PFR. This in turn may produce a CIG overload in the event of a frequency disturbance. By contrast, the damping and PFR of the PI-VSG are fully decoupled and thus can be set independently. Second, due to the larger damping, the dynamic response of the S-VSG to a reference step change is

slower than that of the PI-VSG, as shown in Fig. 3. Therefore, the damping coefficient required for the S-VSG must be used considering a trade-off among the required synchronization stability margins, PFR, and dynamic response.

Regarding the ICLs, they must be considered to assess the synchronization stability of grid-forming VSGs, as evidenced in the conducted small-signal analysis. The analytical results reveal that the grid-forming VSGs adopting OL-ICL exhibit a superior performance, regardless of the selected OCL, as shown in Fig. 8. Nevertheless, the OL-ICL lacks control capability over the VSC voltage and current. Therefore, the alternative and non-straightforward protection schemes are required to protect the grid-forming CIG from overloads and/or overvoltage. This limitation does not apply to the VC-ICL and CC-ICL, which can effectively control the VSC voltage and current, respectively, when properly tuned. Note that each ICL computes the active and reactive power of the grid-forming CIG at different nodes. As a result, only the CC-ICL ensures that the reference power of the grid-forming VSG are injected into the POI.

Finally, Table V summarizes the main properties of each grid-forming VSG, including synchronization stability and other properties based on the proposed systematic procedure.

TABLE V
SYNCHRONIZATION STABILITY AND OTHER PROPERTIES OF GRID-FORMING VSGS

VSG	Stability	HV grid	MV grid	LV grid	Property
S-OL	Well-damped oscillation modes	✓	✓	✓	+Inertial response –Coupled damping and PFR –Lack of voltage or current control
S-VC	Well-damped oscillation modes	✓	✓	✓	+Inertial response –Coupled damping and PFR +Voltage control +Inverter current control
S-CC	1) No low-frequency critical oscillation modes 2) Poorly-damped high-frequency oscillation modes with low <i>SCR</i> 3) Robustness with high <i>SCR</i>	✓	✓	×	+Inertial response –Coupled damping and PFR + <i>PQ</i> control at the POI +Grid current control
PI-OL	1) Well-damped oscillation modes 2) Robustness with low <i>SCR</i>	✓	✓	✓	+Inertial response +Decoupled damping and PFR +Faster time response –Lack of voltage or current control
PI-VC	1) Poorly-damped low-frequency oscillation mode with high <i>SCR</i> and low <i>R/X</i> 2) Robustness with low <i>SCR</i>	×	✓	✓	+Inertial response +Decoupled damping and PFR +Faster time response +Voltage control +Inverter current control
PI-CC	1) No low-frequency critical oscillation mode 2) Poorly-damped high-frequency oscillation modes with low <i>SCR</i> 3) Robustness with high <i>SCR</i>	✓	✓	×	+Inertial response +Decoupled damping and PFR +Faster time response + <i>PQ</i> control at the POI +Grid current control

Note: the symbol ✓ represents that the grid-forming VSG is applicable to HV, MV, or LV grid; the symbol × represents that the grid-forming VSG is not applicable to HV, MV, or LV grid; the symbol + represents the advantages; and the symbol – represents the disadvantages.

VI. CONCLUSION

This study proposes a systematic small-signal analysis procedure to evaluate and improve the synchronization stability of grid-forming VSGs. The proposed systematic procedure is applied to six grid-forming VSGs, derived using different combinations of OCL and ICL blocks. Given that the synchronization stability is extremely sensitive to power system characteristics, the analysis considers a wide range of *SCR* and *R/X* to draw general conclusions.

The proposed systematic procedure enhances the synchronization stability of grid-forming VSGs, providing insights into how controller gains should be re-tuned for this purpose. The application of the proposed systematic procedure reveals that the S-VSG, parameterized according to state-of-the-art practices, has a broader stable region as compared with PI-VSG. This is caused by a large damping coefficient, which is required because of the POI characteristics. This parameter may lead to a slower transient response and a larger PFR, which could cause a CIG overload in the event of a frequency disturbance. In addition, the ICLs play a crucial role in the stability of grid-forming VSGs. For the ICLs based on voltage control, i.e., VC-ICL and OC-ICL, the stability is determined by low-frequency oscillation modes associated with the APCL. By contrast, the stability of grid-forming VSGs with ICLs based on current control, i.e., CC-ICL, is linked to high-frequency oscillation modes associated with the current controller. Therefore, the synchronization stability of grid-forming VSGs does not solely depend on low-frequency modes as traditionally defined, as high-frequency modes can also emerge due to the rapid control actions with-

in the ICLs. Finally, VC-ICL and OC-ICL are more suitable for networks with medium/low *SCR*, whereas CC-ICL is more effective for networks with medium/high *SCR*. In general, a high *R/X* improves stability across all grid-forming VSGs, as expected.

Future research will focus on extending this systematic analysis to other aspects of grid-forming VSGs, including power system dynamics and unbalanced operation.

REFERENCES

- [1] J. M. Maza-Ortega, E. Acha, S. García *et al.*, “Overview of power electronics technology and applications in power generation transmission and distribution,” *Journal of Modern Power Systems and Clean Energy*, vol. 5, no. 4, pp. 499-514, Jul. 2017.
- [2] H. Bevrani, H. Golpîra, A. R. Messina *et al.*, “Power system frequency control: an updated review of current solutions and new challenges,” *Electric Power Systems Research*, vol. 194, p. 107114, May 2021.
- [3] H. Gu, R. Yan, and T. K. Saha, “Minimum synchronous inertia requirement of renewable power systems,” *IEEE Transactions on Power Systems*, vol. 33, no. 2, pp. 1533-1543, Mar. 2018.
- [4] N. Hatziaargyriou, J. Milanovic, C. Rahmann *et al.*, “Definition and classification of power system stability – revisited & extended,” *IEEE Transactions on Power Systems*, vol. 36, no. 4, pp. 3271-3281, Jul. 2021.
- [5] D. Liu, X. Zhang, and C. K. Tse, “Effects of high level of penetration of renewable energy sources on cascading failure of modern power systems,” *IEEE Journal on Emerging and Selected Topics in Circuits and Systems*, vol. 12, no. 1, pp. 98-106, Mar. 2022.
- [6] H. Zhang, W. Xiang, W. Lin *et al.*, “Grid forming converters in renewable energy sources dominated power grid: control strategy, stability, application, and challenges,” *Journal of Modern Power Systems and Clean Energy*, vol. 9, no. 6, pp. 1239-1256, Nov. 2021.
- [7] R. Rosso, X. Wang, M. Liserre *et al.*, “Grid-forming converters: control approaches, grid-synchronization, and future trends – a review,” *IEEE Open Journal of Industry Applications*, vol. 2, pp. 93-109, Apr. 2021.

- [8] D. Sun, H. Liu, S. Gao *et al.*, "Comparison of different virtual inertia control methods for inverter-based generators," *Journal of Modern Power Systems and Clean Energy*, vol. 8, no. 4, pp. 768-777, Jul. 2020.
- [9] H. Xin, L. Huang, L. Zhang *et al.*, "Synchronous instability mechanism of P - f droop-controlled voltage source converter caused by current saturation," *IEEE Transactions on Power Systems*, vol. 31, no. 6, pp. 5206-5207, Nov. 2016.
- [10] L. Zhang, L. Harnefors, and H. P. Nee, "Power-synchronization control of grid-connected voltage-source converters," *IEEE Transactions on Power Systems*, vol. 25, no. 2, pp. 809-820, May 2010.
- [11] M. Ndreko, S. Rüberg, and W. Winter, "Grid forming control for stable power systems with up to 100% inverter based generation: a paradigm scenario using the IEEE 118-bus system," in *Proceedings of 17th International Wind Integration Workshop*, Stockholm, Sweden, Oct. 2018, pp. 1-6.
- [12] S. Dong and Y. Chen, "Adjusting synchronverter dynamic response speed via damping correction loop," *IEEE Transactions on Energy Conversion*, vol. 32, no. 2, pp. 608-619, Jun. 2017.
- [13] P. Rodríguez, C. Citro, J. I. Candela *et al.*, "Flexible grid connection and islanding of SPC-based PV power converters," *IEEE Transactions on Industry Applications*, vol. 54, no. 3, pp. 2690-2702, May 2018.
- [14] M. Chen, D. Zhou, and F. Blaabjerg, "Modelling, implementation, and assessment of virtual synchronous generator in power systems," *Journal of Modern Power Systems and Clean Energy*, vol. 8, no. 3, pp. 399-411, May 2020.
- [15] G. C. Kryonidis, K. N. D. Malamaki, J. M. Mauricio *et al.*, "A new perspective on the synchronverter model," *International Journal of Electrical Power & Energy Systems*, vol. 140, p. 108072, Sept. 2022.
- [16] A. J. Roscoe, M. Yu, A. Dyško *et al.*, "A VSM (virtual synchronous machine) converter control model suitable for RMS studies for resolving system operator/owner challenges," in *Proceedings of 15th Wind Integration Workshop*, Vienna, Austria, Nov. 2016, pp. 1-8.
- [17] D. Remon, A. M. Cantarellas, E. Rakhshani *et al.*, "An active power synchronization control loop for grid-connected converters," in *Proceedings of 2014 IEEE PES General Meeting*, National Harbor, USA, Jul. 2014, pp. 1-5.
- [18] M. Ndreko, S. Rüberg, and W. Winter, "Grid forming control scheme for power systems with up to 100% power electronic interfaced generation: a case study on Great Britain test system," *IET Renewable Power Generation*, vol. 14, no. 8, pp. 1268-1281, Jun. 2020.
- [19] C. Li, Y. Yang, Y. Cao *et al.*, "Frequency and voltage stability analysis of grid-forming virtual synchronous generator attached to weak grid," *IEEE Journal of Emerging and Selected Topics in Power Electronics*, vol. 10, no. 3, pp. 2662-2671, Jun. 2022.
- [20] J. C. Olives-Camps, J. M. Mauricio, M. Barragán-Villarejo *et al.*, "Voltage control of four-leg VSC for power system applications with nonlinear and unbalanced loads," *IEEE Transactions on Energy Conversion*, vol. 35, no. 2, pp. 640-650, Jun. 2020.
- [21] P. Rodríguez, I. Candela, C. Citro *et al.*, "Control of grid-connected power converters based on a virtual admittance control loop," in *Proceedings of 2013 15th European Conference on Power Electronics and Applications*, Lille, France, Sept. 2013, pp. 1-10.
- [22] G. C. Kryonidis, J. M. Mauricio, K. N. D. Malamaki *et al.*, "Use of ultracapacitor for provision of inertial response in virtual synchronous generator: design and experimental validation," *Electric Power Systems Research*, vol. 223, p. 109607, Oct. 2023.
- [23] F. J. Matas-Díaz, M. Barragán-Villarejo, J. C. Olives-Camps *et al.*, "Virtual conductance based cascade voltage controller for VSCs in islanded operation mode," *Journal of Modern Power Systems and Clean Energy*, vol. 10, no. 6, pp. 1704-1713, Nov. 2022.
- [24] T. Qoria, F. Gruson, F. Colas *et al.*, "Tuning of cascaded controllers for robust grid-forming voltage source converter," in *Proceedings of 2018 Power Systems Computation Conference*, Dublin, Ireland, Jun. 2018, pp. 1-7.
- [25] Z. Liu, J. Liu, D. Boroyevich *et al.*, "Small-signal terminal-characteristics modeling of three-phase droop-controlled inverters," in *Proceedings of 2016 IEEE Energy Conversion Congress and Exposition*, Milwaukee, USA, Sept. 2016, pp. 1-7.
- [26] S. J. Yague, A. García-Cerrada, and P. P. Farré, "Comparison between modal analysis and impedance-based methods for analysing stability of unbalanced microgrids with grid-forming electronic power converters," *Journal of Modern Power Systems and Clean Energy*, vol. 11, no. 4, pp. 1269-1281, Jul. 2023.
- [27] X. Wang and F. Blaabjerg, "Harmonic stability in power electronic-based power systems: concept, modeling, and analysis," *IEEE Transactions on Smart Grid*, vol. 10, no. 3, pp. 2858-2870, May 2019.
- [28] J. Yu, S. Wang, Z. Liu *et al.*, "Accurate small-signal terminal characteristic model and SISO stability analysis approach for parallel grid-forming inverters in islanded microgrids," *IEEE Transactions on Power Electronics*, vol. 38, no. 5, pp. 6597-6612, May 2023.
- [29] M. H. Ravanji, D. B. Rathnayake, M. Z. Mansour *et al.*, "Impact of voltage-loop feedforward terms on the stability of grid-forming inverters and remedial actions," *IEEE Transactions on Energy Conversion*, vol. 38, no. 3, pp. 1554-1565, Sept. 2023.
- [30] X. Gao, D. Zhou, A. Anvari-Moghaddam *et al.*, "A comparative study of grid-following and grid-forming control schemes in power electronic-based power systems," *Power Electronics and Drives*, vol. 8, no. 1, pp. 1-20, Jan. 2023.
- [31] X. Gao, D. Zhou, A. Anvari-Moghaddam *et al.*, "Stability analysis of grid-following and grid-forming converters based on state-space model," in *Proceedings of 2022 International Power Electronics Conference*, Himeji, Japan, May 2022, pp. 422-428.
- [32] X. Gao, D. Zhou, A. Anvari-Moghaddam *et al.*, "Stability analysis of grid-following and grid-forming converters based on state-space modeling," *IEEE Transactions on Industry Applications*, vol. 60, no. 3, pp. 4910-4920, May 2024.
- [33] W. Wang, X. Shi, G. Wu *et al.*, "Interaction between grid-forming converters with AC grids and damping improvement based on loop shaping," *IEEE Transactions on Power Systems*, vol. 39, no. 1, pp. 1905-1917, Jan. 2024.
- [34] F. Zhao, T. Zhu, L. Harnefors *et al.*, "Closed-form solutions for grid-forming converters: a design-oriented study," *IEEE Open Journal of Power Electronics*, vol. 5, pp. 186-200, Jan. 2024.
- [35] O. Damanik, Ö. C. Sakinci, G. Grdenić *et al.*, "Evaluation of the use of short-circuit ratio as a system strength indicator in converter-dominated power systems," in *Proceedings of 2022 IEEE PES Innovative Smart Grid Technologies Conference Europe*, Novi Sad, Serbia, Oct. 2022, pp. 1-5.
- [36] C. Henderson, A. Egea-Alvarez, T. Kneuppel *et al.*, "Grid strength impedance metric: an alternative to SCR for evaluating system strength in converter dominated systems," *IEEE Transactions on Power Delivery*, vol. 39, no. 1, pp. 386-396, Feb. 2024.
- [37] R. Aljarrah, B. B. Fawaz, Q. Salem *et al.*, "Issues and challenges of grid-following converters interfacing renewable energy sources in low inertia systems: a review," *IEEE Access*, vol. 12, pp. 5534-5561, Jan. 2024.
- [38] M. B. Frasetyo, F. D. Wijaya, and E. Firmansyah, "Review on virtual synchronous generator model and control for improving microgrid stability," in *Proceedings of 2021 7th International Conference on Electrical Energy Systems*, Chennai, India, Feb. 2021, pp. 397-402.
- [39] Y. Lamrani, F. Colas, T. van Cutsem *et al.* (2024, Jan.). A comparative study of grid-forming controls and their effects on small-signal stability. [Online]. Available: <https://www.techrxiv.org/doi/full/10.36227/techrxiv.22006310.v2Jan.2024>.
- [40] K. Mahmoud, P. Astero, P. Peltoniemi *et al.*, "Promising grid-forming VSC control schemes toward sustainable power systems: comprehensive review and perspectives," *IEEE Access*, vol. 10, pp. 130024-130039, Dec. 2022.
- [41] Y. Li, Y. Xia, Y. Ni *et al.*, "Transient stability analysis for grid-forming VSCs based on nonlinear decoupling method," *Sustainability*, vol. 15, no. 15, p. 11981, Aug. 2023.
- [42] F. J. Matas-Díaz, M. Barragán-Villarejo, J. M. Maza-Ortega *et al.*, "Active harmonic filtering with selective overcurrent limitation for grid-forming VSCs: stability analysis and experimental validation," *IEEE Transactions on Industry Applications*, vol. 60, no. 3, pp. 4762-4775, May 2024.
- [43] L. Huang, C. Wu, D. Zhou *et al.*, "Impact of virtual admittance on small-signal stability of grid-forming inverters," in *Proceedings of 2021 6th IEEE Workshop on the Electronic Grid*, New Orleans, USA, Nov. 2021, pp. 1-8.
- [44] *IEEE Guide for Planning DC Links Terminating at AC Locations Having Low Short-circuit Capacities*, IEEE Std 1204-1997, pp. 1-216, 1997.
- [45] *IEEE Recommended Practice and Requirements for Harmonic Control in Electric Power Systems*, IEEE Std 519-2014 (Revision of IEEE Std 519-1992), pp. 1-29, 2014.

Francisco Jesús Matas-Díaz received the B.S. degree in aerospace engineering, the Master degree in power systems, and the Ph.D. degree in electrical engineering from the University of Seville, Seville, Spain, in 2017, 2020, and 2024, respectively, where he is currently a Research Assistant at the Department of Electrical Engineering. His research interests include con-

trol of power converters and provision of ancillary services related to power quality, hardware-in-the-loop (HIL) testing, and experimental validation of power converters.

Manuel Barragán-Villarejo received the B.S. and Ph.D. degrees in electrical engineering from the University of Seville, Seville, Spain, in 2008 and 2014, respectively. Since 2008, he has been with the Department of Electrical Engineering, University of Seville, where he is currently an Associate Professor. His research interests include exploitation and control of power

converters for smart grid management and grid integration of distributed renewable energy sources.

José María Maza-Ortega received the B.S. and Ph.D. degrees from the University of Seville, Seville, Spain, in 1996 and 2001, respectively. Since 1997, he has been with the Department of Electrical Engineering, University of Seville, where he is currently a Full Professor. His research interests include power quality, harmonic filter, integration of renewable energies, and power electronics.